

Microstructural Ordering of Nanofibers in Flow-Directed Assembly

Enlai Gao^{1,4}, Shijun Wang^{1,4}, Chuanhua Duan^{2,*} and Zhiping Xu^{1,3,*}

¹Applied Mechanics Laboratory, Department of Engineering Mechanics, and Center for Nano and Micro Mechanics, Tsinghua University, Beijing 100084, China

²Department of Mechanical Engineering, Boston University, Boston, MA 02215, USA

³Applied Mechanics and Structure Safety Key Laboratory of Sichuan Province, School of Mechanics and Engineering, Southwest Jiaotong University, Chengdu 611756, China

⁴These authors contribute equally to this work.

*Corresponding authors. Emails: xuzp@tsinghua.edu.cn, duan@bu.edu

Abstract

Fabrication of highly ordered and dense nanofibers assemblies is of key importance for high-performance and multi-functional material and device applications. In this work, we design an experimental approach *in silico*, where shear flow and solvent evaporation are applied to tune the alignment, overlap of nanofibers, and density of the assemblies. Microscopic dynamics of the process is probed by dissipative particle dynamics simulations, where hydrodynamic and thermal fluctuation effects are fully modeled. We find that microstructural ordering of the assembled nanofibers can be established within a specific range of the Peclet numbers and evaporation rates, while the properties of nanofibers and their interaction are crucial for the local stacking order. The underlying mechanisms are elucidated by considering the competition between hydrodynamic coupling and thermal fluctuation. Based on these understandings, a practical design of flow channels for nanofiber assembly with promising mechanical performance is outlined.

Keywords nanofiber, nanostructured assemblies, shear flow, solvent evaporation, alignment, stacking order, densification, dissipative particle dynamics

1. Introduction

Low-dimensional nanostructures such as nanowires, nanotubes and nanosheets can be utilized as elementary building blocks in constructing high-performance, multi-functional materials and devices [1, 2]. The advantages of this bottom-up approach include function-oriented structural tailoring and engineering from the molecular and microstructural levels up to macroscopic scales where materials are usually used. However, to harness remarkable and unconventional attributes of nanostructures to a macroscopical material or device is highly challenging. A significant number of theoretical models have been proposed to elucidate the correlation between microstructures (alignment, overlap, density, etc.) of nanofiber assemblies and their macroscopic performance [3-8]. Rationally optimizing their microstructures becomes the core idea in this new dimension of design, but experimental advances along the direction are retarded due to the lack of precise and efficient control of the organization of the building blocks in their assemblies. Insights from theoretical investigation have been offered to understand these processes. For example, it is worth noting that although directed self-assembly could be tuned to obtain nanofiber networks with various topology, ranging from lattices to liquid-crystal-like microstructures, the lack of directional driven force cannot assure the production of dense and ordered microstructures for high material performance. As a result, sparse networks with considerable local topological defects of nanofiber assemblies form during their directed self-assembly process [9].

One powerful way to assemble nanofibers with outstanding mechanical properties is the process inspired by spider silk spinning in Mother Nature, with dry, wet, melting and other spinning techniques as its industrial counterparts [10, 11]. Fibers, sheets or other building blocks are dispersed into solvents, and then exposed to uniaxial viscous flow with solvent evaporated to improve microstructural orders [12, 13]. Spinning and filtration techniques have also been widely adopted to assemble fibers and membranes from nanofibers and nanosheets, which are

promising as new classes of engineering materials with enhanced mechanical, thermal, electrical and optical properties [14-16]. However, the quality of assembled structures and understanding of the underlying mechanisms at the microstructural level need to be further improved [7, 13, 17]. Recently, three-dimensional (3D) printing technology has also been applied to fabricate structures with well-aligned or hierarchical microstructures [18, 19]. However, microstructural ordering and control of these processes remain to be elucidated, and have to be well understood to fabricate materials and devices with desired performance.

To understand flow-driven motion of microstructures, studies have been carried out for the orientational dynamics of ellipsoid and cylinders. Jeffrey [20] developed theories that predict the behaviors of a rigid ellipsoid or cylinder exposed to hydrodynamic forces only, in the absence of Brownian motion [21]. The ellipsoid undergoes an orbital motion in viscous flow, and the trajectory is known later as the Jeffery orbit. Computer simulations and experiments were conducted to explore these orbits by considering the Brownian motion of a single cylinder, which suggest that orientation of the cylinder prefers to be spatially homogeneous due to thermal fluctuation [22-25]. Tannous [26] showed that the two-dimensional (2D) probability density functions (PDFs) of cylinders satisfies the Fokker-Planck equation, and the driven flow improves the orientational order of the assemblies. Rigid solid objects align to the direction of shear flow and the orientation order can be expressed as function of the Peclet number, $Pe = \dot{\gamma}/D_r$, where $\dot{\gamma}$ is the shear rate and D_r is the rotational diffusion coefficient [27]. Moreover, in a recent experimental study, the relaxation of flow-induced orientation of multiwalled carbon nanotubes (CNTs) was observed following flow cessation [28], although detailed correlation between the flow-structure interaction (*e.g.* properties of the fluid, flow rate, nanofiber concentration, shape and interaction) and the assembled structures still awaits clarification. For assemblies with well-aligned nanofibers, inter-fiber load transfer is limited by the interfacial shear resistance, that is determined by their spatial overlap if the assembly fails at the interfaces [4]. However, up to now, interfiber overlap or the end alignment of nanofibers in their assemblies are rarely

discussed due to the difficulty in both control and characterization.

In addition to fiber alignment and overlap, the packing density is another key figure of merit in the assembly process. Solvent evaporation is one general route to make the nanofibers well-aligned and densely packed [2, 29]. Marin and his collaborators [30, 31] demonstrated an order-to-disorder transition of particles in coffee-ring stains as an evaporation-induced assembly process. Bigioni *et al.* and Narayanan *et al.* [32, 33] showed that relative time scales of particle accumulation and diffusion determine the assembling behavior and growth kinetics of monolayer gold nano-particles. Experiments were conducted by applying solvent evaporation to assemble superstructures [29, 34]. However, the synergistic effect of shear flow and evaporation on highly ordered and dense assembly structures has not been well addressed.

Our understanding of how to precisely assemble highly ordered and dense assembly structures through shear flow and solvent evaporation need to be advanced, for example, with knowledge and insights from their microscopic dynamics. To this end, here we present a numerical study based on dissipative particle dynamics (DPD) simulations for the flow- and evaporation-induced assembly process of nanofibers in liquid. We consider factors that influence the assembled structure such as the shear rate of flow, properties of the fluid, geometry and properties of the nanofibers, evaporation kinetics, as well as the nanofiber-nanofiber, nanofiber-fluid interactions. Based on the findings, we identify the viable conditions for aligned, densely-packed nanofiber assemblies with specific inter-fiber overlap, and propose a practical design of the fluidic channel.

2. Models and methods

In this work, we model the flow- and evaporation-driven assembly of nanofibers using 2D DPD simulations, which is a mesoscale particle-based coarse-graining simulation method [35, 36]. DPD is demonstrated to be powerful in exploring the dynamic and rheological properties of simple or complex fluids at the microscopic level [37]. A direct two-way coupling between the fluid (diffusion, flow) and

structures (deformation, dynamics) are included in the simulations. The motion of the DPD beads is governed by Newton's equations, and the force on particle can be decomposed into three parts of contributions

$$F_i = \sum_{j \neq i} (F_{ij}^C + F_{ij}^D + F_{ij}^R) \quad (1)$$

Here C , D , and R stand for conservative, dissipative, and random, respectively. For a bead in the single-component DPD, the forces exerted on particle i by particle j include

$$F_{ij}^C = a(1 - r_{ij}/R_c)\hat{\mathbf{r}}_{ij}, r_{ij} < R_c \quad (2)$$

$$F_{ij}^D = -\gamma w^D(r_{ij})(\hat{\mathbf{r}}_{ij} \cdot \mathbf{v}_{ij})\hat{\mathbf{r}}_{ij} \quad (3)$$

$$F_{ij}^R = \sigma_R w^R(r_{ij})\theta_{ij}\hat{\mathbf{r}}_{ij} \quad (4)$$

Here $\mathbf{v}_{ij} = \mathbf{v}_i - \mathbf{v}_j$, $\mathbf{r}_{ij} = \mathbf{r}_i - \mathbf{r}_j$, $r_{ij} = |\mathbf{r}_{ij}|$ and $\hat{\mathbf{r}}_{ij} = \mathbf{r}_{ij}/r_{ij}$. The conservative force F_{ij}^C is a soft repulsion acting along the line of bead centers and $a = a_{ij} = (a_i a_j)^{1/2}$, where a_i and a_j are conservative force coefficients for particles i and j , and R_c is the cut-off distance for this soft repulsion. The coefficients γ in F_{ij}^D and σ_R in F_{ij}^R define the amplitudes of the dissipative and random forces, respectively. w^D and w^R are weight functions that vanish for $r_{ij} > R_c$, and θ_{ij} is a Gaussian random variable that satisfies $\langle \theta_{ij}(t) \rangle = 0$ and $\langle \theta_{ij}(t)\theta_{kl}(t') \rangle = (\delta_{ik}\delta_{jl} + \delta_{il}\delta_{jk})\delta(t - t')$. To ensure that the Boltzmann distribution is achieved at thermal equilibrium, we require $w^D(r_{ij}) = [w^R(r_{ij})]^2$ and $\sigma^2 R = 2\gamma k_B T$. For simplicity, $w^D(r_{ij})$ is chosen to be $1 - r_{ij}/R_c$, which defines the same interaction region as that for the conservative force.

We coarse grain both solvent and nanofibers in the DPD simulations. For the solvent, nine water molecules are grouped into one bead. The molecular volume of water is $v_w = 30 \text{ \AA}^3$, so that one bead represents the volume of $V_w = 270 \text{ \AA}^3$. The number density of DPD beads is chosen to be $\rho R_c^3 = 3$, where ρ is the number of DPD beads per cubic volume R_c^3 . Accordingly, we have $R_c = 9.32 \text{ \AA}$ and $m = 2.69 \times 10^{-25} \text{ kg}$. The DPD time scale for the assembly dynamics, $\tau = 549 \text{ ps}$, is obtained by matching the bulk diffusion constant of water [35]. In the DPD simulations, we use R_c , $k_B T$, m and τ as the reference units for length, energy, mass and time [38]. The value of parameter a is fitted to reproduce the solvent compressibility as shown in **Fig. S1** in

the **Supplementary Material**. In summary, these settings are validated by reproducing the mass density, 1000 kg/m^3 , diffusion coefficient, $2.43 \pm 0.01 \times 10^{-5} \text{ cm}^2/\text{s}$, and bulk modulus of water, 2.2 GPa , as summarized in **Table S1**.

For nanofibers, without loss of generality, we use structural and material parameters for typical multi-walled CNTs as adopted in our previous work [9]. The typical length, l , of CNTs in wet-spun fibers is on the order of micrometers [1], much smaller than their persistence length l_p (tens of millimeters for the parameters used here at 300 K), and thus the CNTs are stiff, rod-like fibers during the assembly process in solvent. Although not discussed here, more flexible (thinner or longer, with $l \gg l_p$) CNTs are expected to bend and even collapse in the solvent, leading to more complicate dynamics (*e.g.* forming self-adhesion contact, entanglement with other CNTs) and less ordered microstructures. For each CNT, the stretching contribution between two bonding beads to the total energy is given by $E_T = K_T(R - R_0)^2/2$, where $K_T = YA/2R_0$ is the spring constant related to the tensile stiffness, expressed in the Young's modulus Y , the cross-section area A , and distance between two bonding beads R . R_0 is the equilibrium inter-bead distance. The bending energy contribution within an adjacent beads triplet is described as $E_B = K_B(1 + \cos\theta)$, where $K_B = 3YI/2R_0$ is the angular spring constant related to the bending stiffness $D = YI$, θ is bending angle within the triplet, and I is the bending moment of inertia. Although the van der Waals cohesion between CNTs, modelled by the Lennard-Jones potential in the 12-6 form with parameters ε and σ , helps them to form bundles in the dry condition, it is screened here in the solvent by the microhydrodynamical effect. In experimental preparation of CNT solution for fiber fabrication, the CNT walls are usually treated by protonation to promote the dispersion process, which effectively eliminates the wall-wall interaction between CNTs [39]. Consequently, we model the inter-fiber and the fiber-solvent interaction in a soft repulsion form (Eq. 2) if not specified, where fiber crossing is prohibited by use a relatively small inter-bead distance in the fiber. As the CNTs are simulated in a bead-chain representation, the CNT-solvent interaction and thus the hydrophobicity of CNTs, cannot be adequately modeled. However, for fiber assembly in solvent, the key

mechanism of fluid-structure interaction is the momentum exchange between the solvent and CNT, which is not expected to depend on the hydrophobicity of CNTs significantly. These force field parameters are summarized in **Table S2**.

All DPD simulations run under the constant-temperature condition at 300 K using the DPD thermostat, which conserves the total momentum of system and correctly captures the hydrodynamics [35, 36]. To maintain the balance between numerical stability and the computational consumption, we use two different time step sizes for the DPD beads of solvent ($\sim 10^5$ beads) and nanofibers ($\sim 10^3$ beads), 0.005τ and 0.0001τ , respectively, which are implemented through the reversible reference system propagator algorithms (rRESPA) multi-timescale integrator with two hierarchical levels [40]. More details can be found in the **Supplementary Material**. Equilibrium molecular dynamics (EMD) simulations are performed to measure the rotational coefficient based on the Einstein relation, by tracking the angular mean square displacement (AMSD). The Lees-Edwards's boundaries conditions are applied to generate the shear flow, so that the same shear rate is applied to the whole system globally. Periodic boundary conditions (PBCs) are applied to the simulation box with a fixed number of nanofibers dispersed in the dilute solution regime, with $c\ell^2 < 1$ in 2D. Here c is the number density of nanofibers [41]. All simulations are performed using the large scale atomic/molecular massively parallel simulator (LAMMPS) [42].

3. Results and discussion

3.1 Orientational ordering

The process of flow-directed assembly is illustrated in **Fig. 1**, where three simulation snapshots summarize the key steps in forming the assemblies. The first step is to disperse nanofibers in solvents with randomly distributed position and orientation. The center of nanofibers is placed in a regular square lattice and slightly perturbed in a random direction. A random orientation is then sampled to construct the model of a whole nanofiber. The second step is to expose them under controlled shear flow, which introduces a high orientational order within the nanofiber

assemblies. The third step is to evaporate the solvent to reach the final assemblies with highly ordered and dense microstructures. These steps are reminiscent of the microstructural transition of rod-like polymers in solvent as their concentration increases, from dilute, semi-dilute solutions to isotropic concentrated and liquid crystalline solutions [39, 43].

To gain more insights into these processes, we analyze the controlling steps of shear flow and evaporation in the assembly process. We define an orientation order parameter (OOP) O to quantify the orientational order of nanofibers in the assembly, which is also named as the nematic order parameter since it is zero for the randomly aligned isotropic phase and one for the perfectly aligned phase, respectively. Consequently, the alignment of nanofibers to the flow direction ($\theta = 0$) is signaled by the saturation of O towards 1, since in 2D we have

$$O = \langle 2\cos^2\theta - 1 \rangle \quad (5)$$

where definition of θ is shown in **Fig. 1c** and **2b**. In the assembly dynamics, orientation of the nanofibers is determined by the competition between hydrodynamic forces and Brownian random perturbation. The Peclet number Pe measures the relative strength of hydrodynamic forces and Brownian forces, that is

$$Pe = \dot{\gamma}/D_r \quad (6)$$

Here the rotational coefficient D_r is measured through the tracked AMSD in equilibrating DPD simulations using the Einstein relation in 2D, *i.e.*

$$D_r = \Delta\theta^2/2t \quad (7)$$

To probe the effect of Brownian forces while keeping other factors fixed, we first consider various lengths of nanofibers, l , in our DPD simulations. The rotational trajectory of nanofibers in equilibration simulations is plotted in **Fig. S4a**, with the AMSD in **Fig. S4b** in the **Supplementary Material**. These results demonstrate the distinct nature of Brownian rotational motion, and that the rotational diffusion coefficient D_r decreases with the increase in the length of nanofibers. To validate that our 2D model is able to capture the key dynamical processes in nanofiber

assembly, a 3D model is constructed by extruding the current 2D model along the third dimension. The results show that the rotational diffusion behaviors are similar in 2D and 3D, which can both well fitted by Eq. 7 (Fig. S5 in the Supplementary Material).

We apply a shear rate of $\dot{\gamma} = 0.01\tau^{-1}$ to the solvent where these nanofibers are dispersed and monitor the PDF of their orientational distribution, as well as the value of O . From the results summarized in Fig. 2, one finds that the PDF of nanofiber orientation distribution becomes sharply peaked around the most probable orientation angle, indicating a certain degree of orientational order. The parameter O plotted in Fig. 4a demonstrates that OOP increases, while D_r decreases as l increases. A similar trend was reported in the previous study of CNTs in argon gas shear flow [22].

We then explore the role of hydrodynamic forces exclusively, by changing the shear rate $\dot{\gamma}$ while keeping other factors fixed. The distribution of nanofiber orientation is peaked around the most probable value, and the OOP increases with the shear rate in the low- Pe region, as shown in Figs. 3 and 4b. However, this trend is reversed as the Peclet number exceeds a critical value of $Pe = \sim 95$. This finding at low Pe values agrees with the analytical and numerical studies by Tannous [26], where inertial effects are excluded. In contrast, the observation in high Pe number region is anomalous as shown in Fig. 4b. To explain this, one should note that the shear flow simulated here includes both dilatation and rotational components, which thus not only enhances the orientation of nanofibers, but also randomizes their orientation by rotating. Therefore, depending on the strength of the shear field, one effect can be dominating the other [44]. At high Pe , the rotational effect controls the assembling dynamics and leads to the anomalous decline of OOP with further increased shear rate. This anomalous region of Peclet number (or shear rate) should be avoided in practical design, and our following discussions in this work only focus on the region of Peclet number that has a positive correlation between the Peclet number and OOP.

Highly ordered nanofiber assemblies can be achieved in a specific range of Peclet

numbers. However, an experimental study reported relaxation of orientational order following shear flow cessation [28]. We confirm this result in our DPD simulation results, which are summarized in **Figs. 5** and **S6**. Our DPD simulation results show that, in the absence of evaporation (**Fig. 5a**), the OOP increases, reaches a constant under shear flow with t increases from 0 to $5 \times 10^3 \tau$, and then relaxes to zero after shear flow cessation after $t = 5 \times 10^3 \tau$. While in the condition that 85% of the solvent is evaporated (**Figs. 5b** and **S6**, details of DPD simulations can be found in the **Supplementary Material**), the orientational order is partially preserved after shear flow cessation. In addition, from the DPD simulation results, we find that the density of oriented nanofiber assemblies in dilute solution is too low to fabricate high-performance materials in fiber or film forms. Although low density of nanofibers reduces local microstructural defects in the assembly process [9], it prevents wide applications because of the poor mechanical, thermal and electrical properties of the assembly. Hence the density and microstructural stability of nanofiber assemblies need to be improved, and solvent evaporation becomes a feasible approach. As solvent evaporation is introduced, the orientational order can be partially preserved even after flow cessation. From the effect of evaporation rates, we conclude from the simulation results that solvent evaporation leads to ordered and stable assemblies as shown in **Fig. 5**.

3.2 Stacking order

Besides orientational order, the stacking order, or interfiber overlap, of flow-directed nanofiber assembly is another dominating factor controlling the capability of interfiber load transfer [4]. To measure the degree of stacking order of an assembly of nanofibers, assumed to have the same length, we define a parameter S from the distribution of interfiber overlap, *i.e.*

$$S = \int f(x)w(x)dx \tag{8}$$

$$w(x) = 1 - |2x - 1| \tag{9}$$

Here x is the normalized overlap between neighboring pairs of nanofibers, with the value ranging from 0 (perfectly end-aligned) and 1 (perfectly half-staggered) (**Fig.**

6a), $f(x)$ is the PDF of x , and $w(x)$ is a weight function. For $S = 0$ or 1 , the PDF is a Dirac delta function, and for a uniformly random distribution of overlap, we have $f(x) = 1$ and $S = 0.5$. As a result, the value of S allows us to characterize the deviation of the end-alignment from the limits of perfectly-end-aligned, perfectly-half-staggered and uniformly random assemblies. For practical consideration, interfiber adhesion could be designed to control the microstructural ordering in the densely-packed assemblies, and thus we introduce a 12-6 Lennard-Jones form of interaction between DPD beads in neighboring nanofibers (Table S2). The DPD simulation results (Fig. 6b) show that the dependence of S on the shear rate $\dot{\gamma}$ is negligible if the interfiber adhesion is absent. However, the value of S increases with $\dot{\gamma}$ as adhesion is on [45]. By elevating the adhesive strength, S significantly decreases (Fig. 6c), implying that the stacking of closely-packed nanofibers becomes more end-aligned. The stacking order also becomes more sensitive to the bending stiffness if the adhesion is activated (Fig. 6d), with the value of S decreasing with D . As a result, interfiber adhesion and bending resistance of the nanofibers favor the formation of assemblies with the ends of nanofibers well aligned, weakening their mechanical properties by limiting the load transfer capacity through interfaces, and should be avoided by choosing the solvent to disperse the nanofibers, for example [1, 39]. On the other hand, with the adhesion turned on, elevating the shear rate could result in an increasing value of S approaching 0.5, with a uniformly random distribution for the overlap and improved interfiber load transfer.

3.3 Practical design

From previous analysis, we conclude that highly ordered and dense assembled structures of nanofiber assemblies can be obtained by controlling flow and evaporation. Based on these understandings, we propose a design of a fluidic channel where the nature of flow and evaporation can be engineered.

The profile of 2D fluidic channel can be described with two profiles as $h(x)$, $-h(x)$ and the local tangent, $\tan\alpha$, as shown in Fig. 7a. The width, pressure and flow rate at the inlet (outlet) are h_1 ($h_2 = \beta h_1$, where $\beta = h_2/h_1$ defines the channel width reduction), p_1 (p_2) and q_1 (q_2), respectively, and the length of channel is L . From the

Navier-Stokes equation for one dimensional and incompressible flow that disregards gravity and inertia forces for the assembly of nanostructures, we have

$$\frac{d^2 u(x, y)}{dy^2} = \frac{dp(x)}{\mu dx} \quad (10)$$

where u and p are the flow velocity and pressure along channel, respectively. This equation can be solved with boundary conditions $u(x, y = \pm h(x)) = 0$ and the equation of continuity, which gives the spatial distribution of flow velocity, pressure, and the correlation between the flow rate q and pressure difference $\Delta p = p_1 - p_2$. Detailed derivation can be found in the **Supplementary Material**.

$$u(x, y) = \frac{\Delta p}{\mu L} \frac{h_1^2 h_2^2}{(h_1 + h_2) h(x)^3} [h(x)^2 - y^2] \quad (11)$$

$$p(x) = p_1 - \frac{[h_1/h(x)]^2 - 1}{(h_1/h_2)^2 - 1} \Delta p \quad (12)$$

$$q(x) = \frac{4dh_1^2 h_2^2}{3\mu L(h_1 + h_2)} \Delta p = q_1 = q_2 \quad (13)$$

Here d is the depth of this 2D channel. The shear rate distribution in the channel can then be calculated from the $u(x, y)$, which strongly affects the orientational order, while the pressure difference Δp and flow rate q could be used in other design steps such as energy consumption and structural stability, as shown in **Figs. S2** and **S3**.

To further consider the effect of evaporation, a supplementary condition is used to satisfy mass conservation of the solvent. In practice, the evaporation could be achieved by use porous walls in the channel, where liquid is extracted. As long as the evaporation rate is lower than the rate of solvent diffusion and flow that are responsible for mass redistribution in the channel, the situation will be the same as we considered in the model analysis. With the assumption that total evaporation rate ($q_e = \lambda A$) is proportional to the flow area swept from the inlet to x along the channel $A = [h_1^2 - h(x)^2]/\tan\alpha$, the coefficient λ defines the intensity of evaporation. Hence, the flow rate of fluid $q(x)$ at position x can then be expressed as

$$q(x) = q_1 - q_e(x) = q_1 - \lambda \frac{h_0^2 - h(x)^2}{\tan \alpha} \quad (14)$$

The distribution of average shear flow rate along the channel significantly affects the orientational order of nanofibers in the flow, which can be simply defined as

$$\dot{\gamma}(x) = \frac{q(x)}{dh(x)^2} \quad (15)$$

By combining Eqs. 14 and 15, we solve $\dot{\gamma}(x)$ and plot the results for $\dot{\gamma}(x)$ in Fig. 7b, where the dash and solid lines indicate the evaporation-absent condition ($q_2 = q_1$) and strong evaporation limit where q_2 at the outlet vanishes ($q_2 \approx 0$, considering the volume of nanofibers is far lower than that of the solvent at the inlet, as the all solvent evaporates along the channel, the outlet flow rate almost vanishes), respectively. Without evaporation, the average shear rate increases along the channel from the inlet to outlet, due to the gradual reduction of channel width h (Fig. 7a). While in the strong evaporation limit, the trend of shear rate distribution along the channel is reversed. As shown before, the orientational order of nanofibers will relax under shear flow cessation or shear rate reduction, so the shear rate at the outlet plays an important role in determining the orientational order of nanofiber assemblies. Furthermore, our discussion is focused on the region of Pe numbers with positive correlation between Pe and the OOP. Hence, the strong evaporation limit is not beneficial for achieving higher orientational order in practice due to the reducing shear rate distribution from the inlet to outlet, and should be prevented in paractical designs. It should be remarked that the setup we consider here is reminiscent of the industrial fiber spinning process to improve the alignment and densification by extensional flow [46]. The contraction flow in the channel we consider here has a strong extensional flow effect, *i.e.* along the centerline the flow velocity increases as the flow direction in the absence of evaporation. This effect could be even stronger if we solve the full Navier-Stokes equations instead of using the lubrication approximation here.

In order to rationally control the orientational order and packing density of the nanofiber assemblies, we predict the correlation between the shear rate for

orientational ordering, density of nanofibers at the outlet and the shape of fluidic channel (the inlet, outlet width and the length of channel), evaporation intensity coefficient λ . The shear rate at outlet $\dot{\gamma}_{out}$ that controls the orientational order of product assemblies can be derived from **Eqs. 14 and 15**

$$\dot{\gamma}_{out} = \frac{q_1 - \lambda(h_1 + h_2)L}{dh_2^2} \quad (16)$$

Here $\lambda(h_1 + h_2)L$ is the evaporation rate from the inlet to outlet. The density of nanofiber assemblies at the outlet ρ_{out} can be related to the evaporation rate $\lambda(h_1 + h_2)L$ and inlet flow rate q_1 . Accordingly, the density of nanofiber assemblies at the outlet ρ_{out} can be defined as

$$\rho_{out} \sim 1/[q_1 - \lambda(h_1 + h_2)L] \quad (17)$$

This indicates that, the higher rate the solvent evaporates in the flow process, the higher density of assembled structure it could reach. The results of **Eqs. 16 and 17** are shown in **Fig. 8a**, from which we can see that, the shear rate and density of nanofiber assemblies at the outlet can be controlled through adjusting the shape of fluidic channel. In general, long channel and small width of outlet, compared to the width of inlet, are advantageous to fabricate highly ordered and dense assemblies of nanofibers. In addition, from **Eqs. 16, 17** and **Fig. 8b**, both the shear rate and density of nanofiber assemblies at the outlet depend on the evaporation intensity coefficient λ , which suggests that the orientational order and density of assemblies can be adjusted through the evaporation intensity coefficient λ . To summarize, **Fig. 8** illustrates the strategy to access specific ranges of density and orientational order of the nanofiber assemblies through adjusting the shape of fluidic channel, evaporation intensity and applied pressure gradient or rate.

4. Conclusion

In this study, we conducted DPD simulations to explore the dynamic processes of flow and evaporation-induced assembly of nanofibers. Admittedly the results presented here are limited as we consider only identical nanofibers with the same geometry (length, diameter) and only water as a solvent is modeled. However, we

corroborate recent findings in the experiments of controllable assembly of nanofibers [13, 28, 30, 34, 47, 48] and explore the key parameters in the process that determine the microstructure of final assembly. The major findings of this work include that the orientational order and density of assembled structure can be well engineered through parametric design of the experimental setup. Specifically, shear flow within a range of Peclet numbers induces fiber alignment and the evaporation process densifies the assembly, enhances alignment and prevents diffusion-driven relaxation of fiber alignment upon cessation of flow. The overlap distribution largely depends on the strength of interfiber adhesion. Elevating the shear rate, reducing adhesion or improving the flexibility of nanofibers can avoid perfectly end-aligned microstructures with insufficient interfiber load transfer and weakened mechanical performance. A wide spectrum of low-dimensional nanostructures such as nanotubes, nanowires, nanosheets, cyclic peptides can be utilized as the fundamental building blocks in constructing hierarchical materials, and our study presents a numerical framework to model the whole fabrication process, offering key insights into the optimization for high-performance materials [48]. Using the methodology here, one can address more practical issues in the wet approach of nanofiber fabrication such as spinning and 3D printing, including the non-uniform distribution of length, diameter of CNTs, the end-to-end alignment of CNTs in the fiber assembly, other solvents such as acids and organic solvents, the rate effect of evaporation, modified inter-CNT interactions through surface functionalization, assembly of 2D nanostructures or 1D/2D hybrids, and the coagulation process to enhance nanofiber orientation by extracting solvent through the nanofiber-solvent interface [49].

This work was supported by the Opening Project of Applied Mechanics and Structure Safety Key Laboratory of Sichuan Province through Grant SZDKF-1601, and the National Natural Science Foundation of China through Grants 11222217 and 11472150. The simulations were performed on the Explorer 100 cluster system of Tsinghua National Laboratory for Information Science and Technology [50].

FIGURES AND FIGURE CAPTIONS

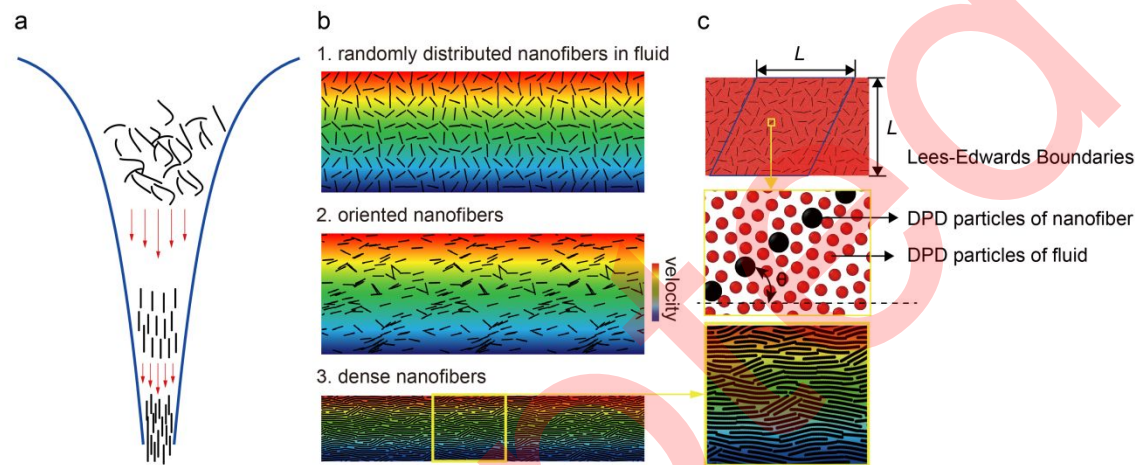


Figure 1 (a) A schematic illustration of the flow-evaporation process for nanofiber assembly. (b) DPD simulation snapshots show the alignment and densification of nanofibers. Only nanofibers are plotted, and the color map indicates the amplitude of velocity field in fluid. (c) Detailed snapshots show the Lees-Edwards boundary condition to simulate the shear flow and DPD beads for nanofibers and fluid.

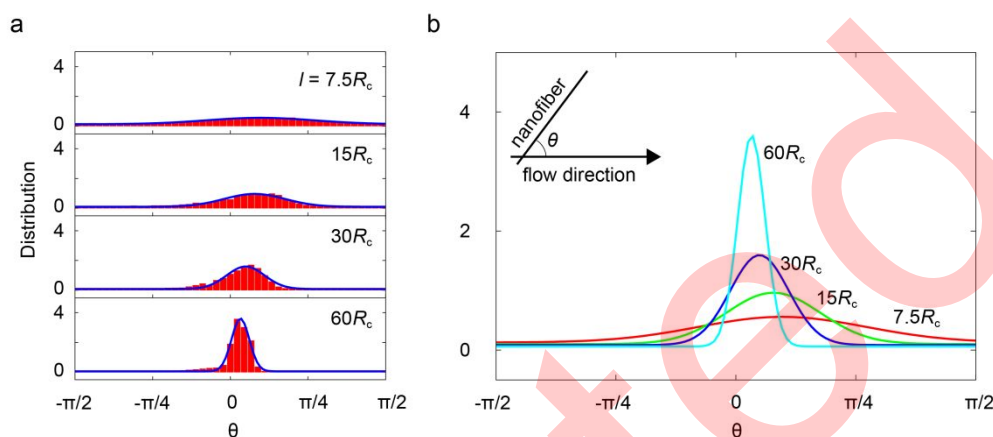


Figure 2 (a) Probability distribution functions (PDFs) of nanofiber orientation. The red boxes are simulation results for different lengths of nanofibers l , fitted to the Gaussian distribution plotted in solid blue lines. (b) Comparison of PDFs shows the increase of the peak value and narrowing of the width as l increases, indicating improved alignment of nanofibers.

1
2
3
4
5
6
7
8
9
10
11
12
13
14
15
16
17
18
19
20
21
22
23
24
25
26
27
28
29
30
31
32
33
34
35
36
37
38
39
40
41
42
43
44
45
46
47
48
49
50
51
52
53
54
55
56
57
58
59
60

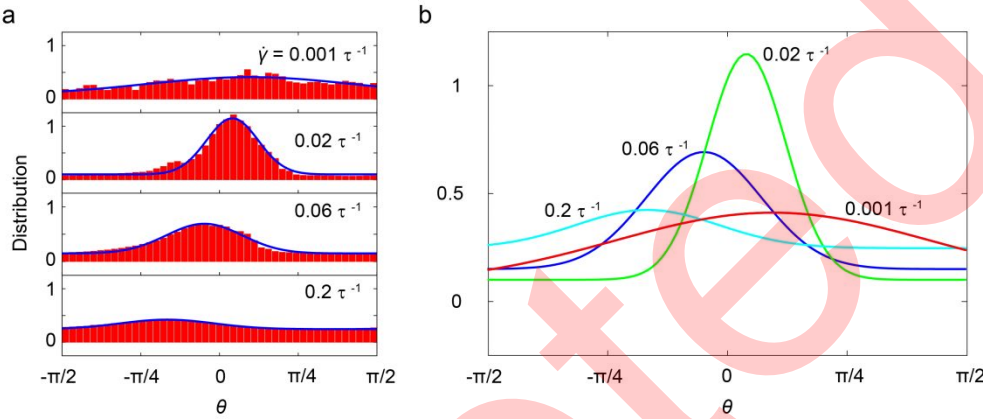


Figure 3 (a) PDFs of nanofiber orientations, plotted for different shear rates $\dot{\gamma}$, which are also fitted to the Gaussian distribution. (b) Comparison between the PDFs shows the shift of the peak value and change in the width as $\dot{\gamma}$ increases.

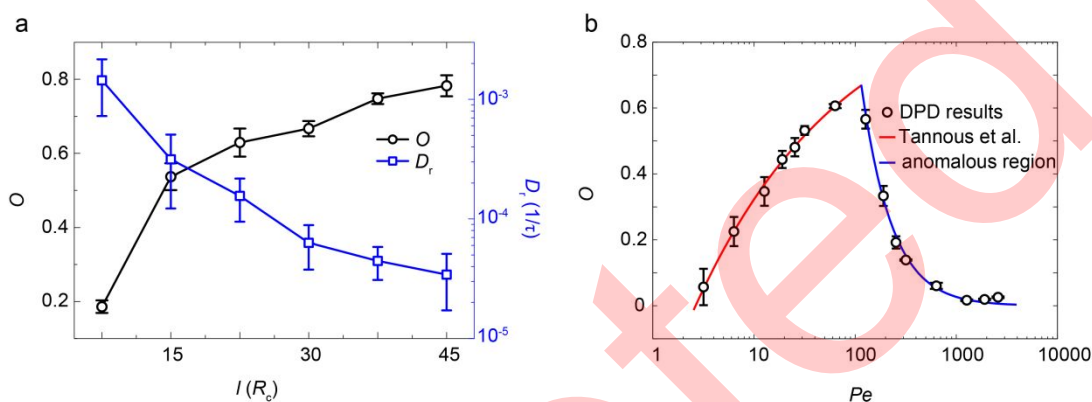


Figure 4 (a) The correlation between the rotational diffusion coefficient D_r , orientational order parameter O , and the length of nanofiber l . Our simulation results show that D_r decreases with l , resulting in a higher Peclet number and increase in O . (b) The correlation between O and the shear rate $\dot{\gamma}$. The value of orientational order parameter O increases first with $\dot{\gamma}$ at the low- Pe regime but decreases after Pe exceeds a critical value of ~ 95 .

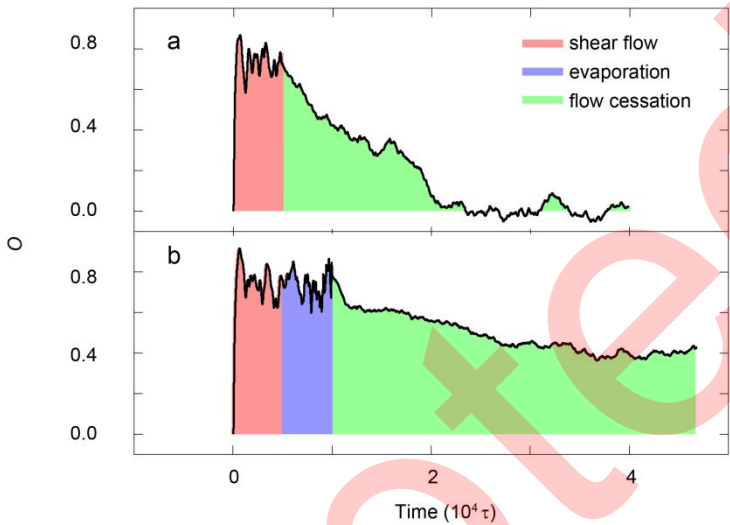


Figure 5 Relaxation of the orientational order in nanofiber assemblies after flow cessation. (a) In the absence of evaporation, the OOP increases, reaching a constant under shear flow ($t = 0 - 5 \times 10^3 \tau$), and then relaxes to zero after shear flow cessation (after $5 \times 10^3 \tau$). (b) With evaporation, the OOP increases and becomes saturated soon. O keeps almost as a constant in $\sim 1 \times 10^4 \tau$, where evaporation (85% of the solvent) is introduced from $t = 5 \times 10^3 \tau$ to $1 \times 10^4 \tau$. After the shear flow cessation from $\sim 1 \times 10^4 \tau$, O relaxes to ~ 0.4 and the orientational order is partially preserved. The light-red, light-blue and light-green regions are the stages of steady shear flow, solvent evaporation and flow cessation, respectively.

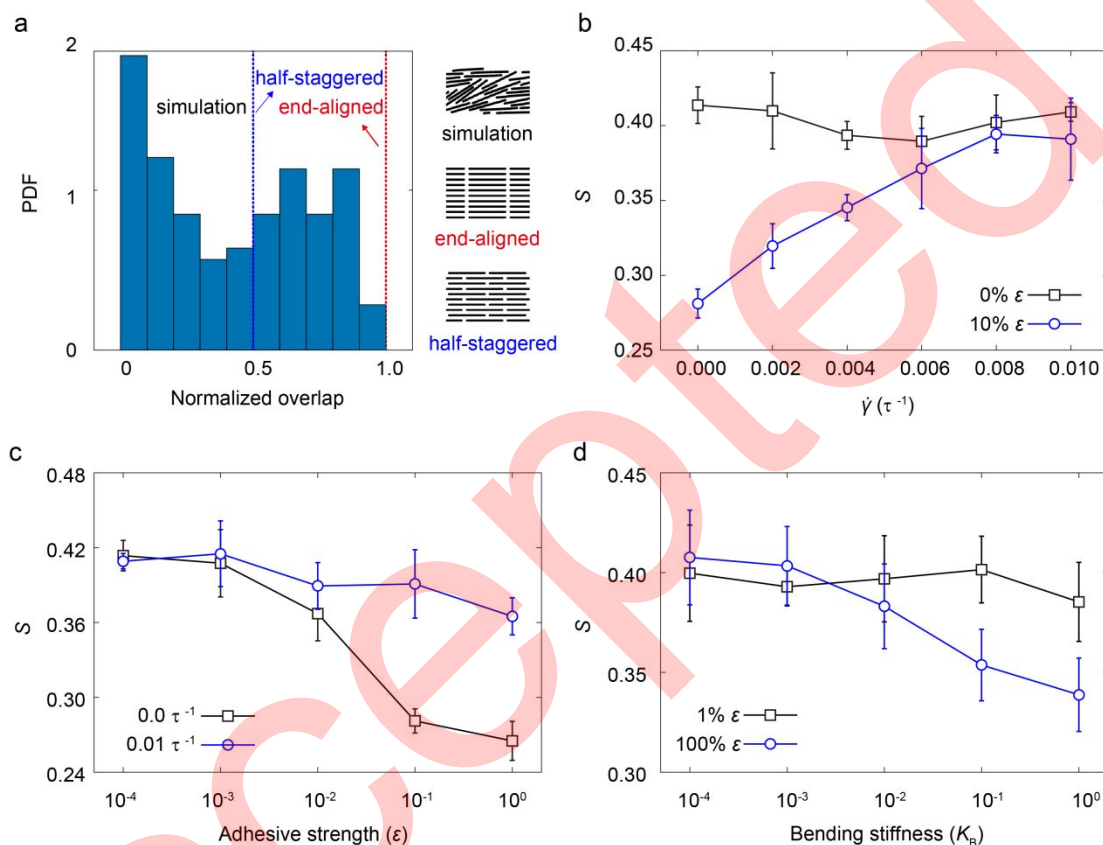


Figure 6 (a) PDF of interfiber overlap measured from DPD simulation results, as well as the perfectly aligned- and half-staggered assemblies. The overlap parameter S plotted as a function of (b) shear rate $\dot{\gamma}$, (c) interfiber adhesive strength measured by the parameter ϵ in the 12-6 Lennard-Jones form of inter-bead interaction, and (d) bending stiffness. Here ϵ and K_B are the potential parameters listed in **Table S2**.

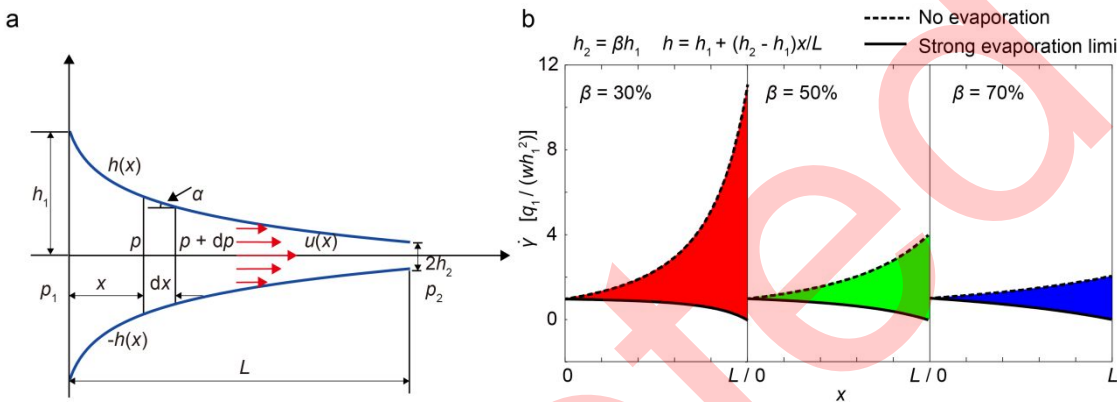


Figure 7 (a) The profile of fluidic channel. (b) Average shear rate distribution along the fluidic channel for different geometrical parameters $\beta = h_2/h_1$. The dash and solid lines show the predictions for the evaporation-absent condition and strong evaporation limit, respectively.

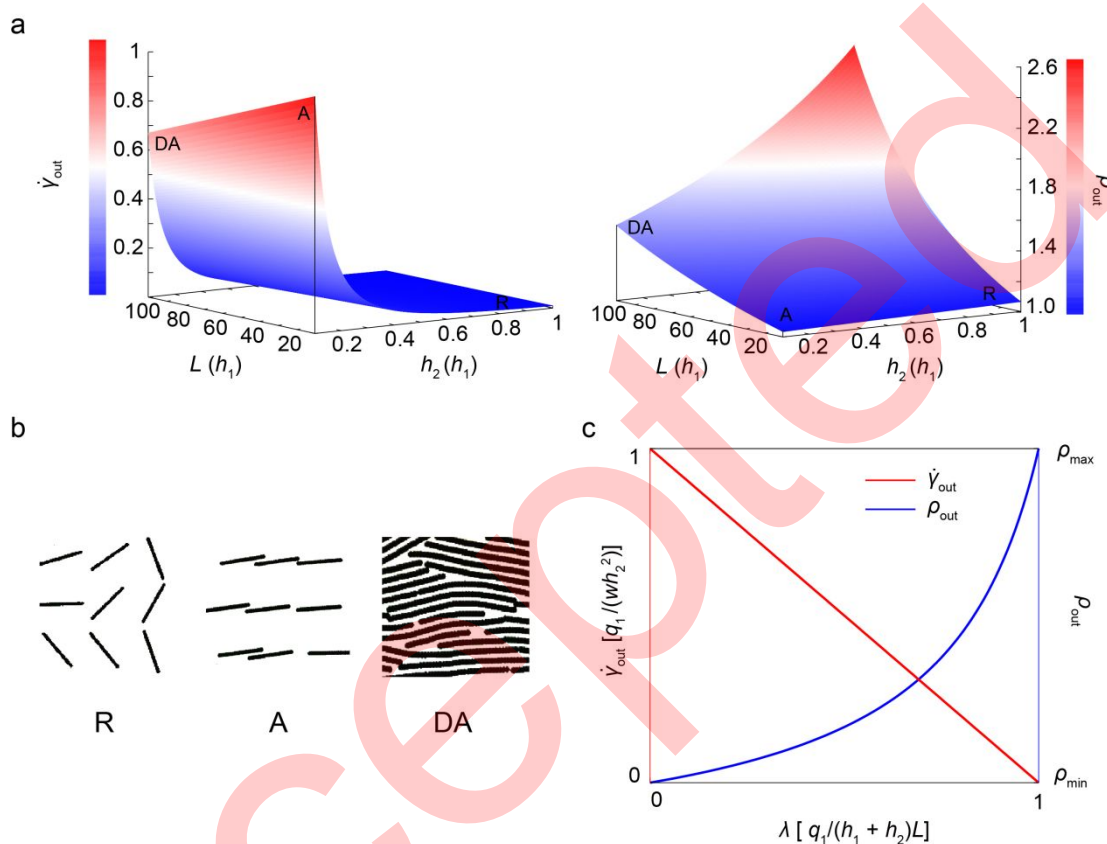


Figure 8 (a) The dependence of outlet shear rate $\dot{\gamma}_{out}$ density ρ_{out} on the shape of fluidic channel, expressed in the ratios of channel length and outlet width to the inlet width, i.e. L/h_1 and h_2/h_1 . The value of $\dot{\gamma}_{out}$ is normalized by its maxima. (b) R, A, and DA stand for the assembly with random, aligned, aligned and densified microstructures obtained from DPD simulations, respectively. (b) The dependence of $\dot{\gamma}_{out}$ and ρ_{out} on the evaporation intensity coefficient λ .

REFERENCES

- 1 Behabtu N, Young C C, Tsentalovich D E, et al. Strong, light, multifunctional fibers of carbon nanotubes with ultrahigh conductivity. *Science*, 2013, 339: 182-186
- 2 Zhang M, Wang Y, Huang L, et al. Multifunctional pristine chemically modified graphene films as strong as stainless steel. *Adv Mater*, 2015, 27: 6708-6713
- 3 Egan P, Sinko R, LeDuc P R, et al. The role of mechanics in biological and bio-inspired systems. *Nat Commun*, 2015, 6: 7418
- 4 Gao E, Lu W and Xu Z. Strength loss of carbon nanotube fibers explained in a three-level hierarchical model. *Carbon*, 2018, 138: 134-142
- 5 Launey M E, Buehler M J and Ritchie R O. On the mechanistic origins of toughness in bone. *Annu Rev Mater Res*, 2010, 40: 25-53
- 6 Liu Y, Xie B, Zhang Z, et al. Mechanical properties of graphene papers. *J Mech Phys Solids*, 2012, 60: 591-605
- 7 Lu W, Zu M, Byun J H, et al. State of the art of carbon nanotube fibers: Opportunities and challenges. *Adv Mater*, 2012, 24: 1805-1833
- 8 Zhu H, Zhu S, Jia Z, et al. Anomalous scaling law of strength and toughness of cellulose nanopaper. *Proc Natl Acad Sci USA*, 2015, 112: 8971-8976
- 9 Xie B, Buehler M J and Xu Z. Directed self-assembly of end-functionalized nanofibers: From percolated networks to liquid crystal-like phases. *Nanotechnology*, 2015, 26: 205602
- 10 Lin S, Ryu S, Tokareva O, et al. Predictive modelling-based design and experiments for synthesis and spinning of bioinspired silk fibres. *Nat Commun*, 2015, 6: 6892
- 11 Rising A and Johansson J. Toward spinning artificial spider silk. *Nat Chem Biol*, 2015, 11: 309-315

- 12 Su B, Wu Y and Jiang L. The art of aligning one-dimensional (1D) nanostructures. *Chem Soc Rev*, 2012, 41: 7832-7856
- 13 Xu Z and Gao C. Graphene in macroscopic order: Liquid crystals and wet-spun fibers. *Acc Chem Res*, 2014, 47: 1267-1276
- 14 Hobbie E K and Fry D J. Nonequilibrium phase diagram of sticky nanotube suspensions. *Phys Rev Lett*, 2006, 97: 036101
- 15 Kwon G, Heo Y, Shin K, et al. Electrical percolation networks of carbon nanotubes in a shear flow. *Phys Rev E*, 2012, 85: 011143
- 16 Shim J S, Yun Y H, Rust M J, et al. The precise self-assembly of individual carbon nanotubes using magnetic capturing and fluidic alignment. *Nanotechnology*, 2009, 20: 325607
- 17 Richardson J J, Bjornmalm M and Caruso F. Technology-driven layer-by-layer assembly of nanofilms. *Science*, 2015, 348: aaa2491
- 18 Gantenbein S, Masania K, Woigk W, et al. Three-dimensional printing of hierarchical liquid-crystal-polymer structures. *Nature*, 2018, 561: 226-230
- 19 Hausmann M K, Ruhs P A, Siqueira G, et al. Dynamics of cellulose nanocrystal alignment during 3D printing. *ACS Nano*, 2018, 12: 6926-6937
- 20 Jeffery G B. The motion of ellipsoidal particles immersed in a viscous fluid. *Proc Roy Soc A*, 1922, 102: 161-179
- 21 Meirson G and Hrymak A N. Two-dimensional long-flexible fiber simulation in simple shear flow. *Polymer Compos*, 2015: 1-9
- 22 Dong R Y and Cao B Y. Anomalous orientations of a rigid carbon nanotube in a sheared fluid. *Sci Rep*, 2014, 4: 6120
- 23 Leal L G and Hinch E J. The effect of weak Brownian rotations on particles in shear flow. *J Fluid Mech*, 1971, 46: 685-703
- 24 Sader J E, Pepperell C J and Dunstan D E. Measurement of the optical properties and shape of nanoparticles in solution using Couette flow. *ACS Nano*,

- 2008, 2: 334-340
- 25 Stover C A, Koch D L and Cohen C. Observations of fibre orientation in simple shear flow of semi-dilute suspensions. *J Fluid Mech*, 2006, 238: 277-296
- 26 Tannous C. Langevin simulations of rod-shaped object alignment by surface flow. *Surf Sci*, 2011, 605: 923-929
- 27 Duggal R and Pasquali M. Dynamics of individual single-walled carbon nanotubes in water by real-time visualization. *Phys Rev Lett*, 2006, 96: 246104
- 28 Pujari S, Rahatekar S S, Gilman J W, et al. Orientation dynamics in multiwalled carbon nanotube dispersions under shear flow. *J Chem Phys*, 2009, 130: 214903
- 29 Brinker C J, Lu Y F, Sellinger A, et al. Evaporation-induced self-assembly: Nanostructures made easy. *Adv Mater*, 1999, 11: 579-585
- 30 Marin A G, Gelderblom H, Lohse D, et al. Order-to-disorder transition in ring-shaped colloidal stains. *Phys Rev Lett*, 2011, 107: 085502
- 31 Marín A G, Gelderblom H, Lohse D, et al. Rush-hour in evaporating coffee drops. *Phys Fluids*, 2011, 23: 091111
- 32 Bigioni T P, Lin X M, Nguyen T T, et al. Kinetically driven self assembly of highly ordered nanoparticle monolayers. *Nat Mater*, 2006, 5: 265-270
- 33 Narayanan S, Wang J and Lin X M. Dynamical self-assembly of nanocrystal superlattices during colloidal droplet evaporation by in situ small angle X-ray scattering. *Phys Rev Lett*, 2004, 93: 135503
- 34 Lee S G, Kim H, Choi H H, et al. Evaporation-induced self-alignment and transfer of semiconductor nanowires by wrinkled elastomeric templates. *Adv Mater*, 2013, 25: 2162-2166
- 35 Groot R D and Rabone K L. Mesoscopic simulation of cell membrane damage, morphology change and rupture by nonionic surfactants. *Biophys J*, 2001, 81: 725-736

- 36 Groot R D and Warren P B. Dissipative particle dynamics: Bridging the gap between atomistic and mesoscopic simulation. *J Chem Phys*, 1997, 107: 4423-4435
- 37 Xu Z, Yang Y, Zhu G, et al. Simulating transport of soft matter in micro/nano channel flows with dissipative particle dynamics. *Adv Theory and Simul*, 2018: 1800160
- 38 Allen M P and Tildesley D J. *Computer Simulation of Liquids*. Clarendon Press (1987).
- 39 Davis V A, Ericson L M, Parra-Vasquez A N G, et al. Phase behavior and rheology of SWNTs in superacids. *Macromolecules*, 2004, 37: 154-160
- 40 Tuckerman M, Berne B J and Martyna G J. Reversible multiple time scale molecular-dynamics. *J Chem Phys*, 1992, 97: 1990-2001
- 41 Hobbie E K. Shear rheology of carbon nanotube suspensions. *Rheologica Acta*, 2010, 49: 323-334
- 42 Plimpton S. Fast parallel algorithms for short-range molecular-dynamics. *J Comput Phys*, 1995, 117: 1-19
- 43 Doi M and Edwards S F. *The Theory of Polymer Dynamics*. Clarendon Press (1988).
- 44 Borzsonyi T, Szabo B, Wegner S, et al. Shear-induced alignment and dynamics of elongated granular particles. *Phys Rev E*, 2012, 86: 051304
- 45 Yang X D, He P F and Gao H J. Competing elastic and adhesive interactions govern deformation behaviors of aligned carbon nanotube arrays. *Appl Phys Lett*, 2012, 101: 053105
- 46 Takajima T. *Advanced Fiber Spinning Technology*. CRC Press (1996).
- 47 Ko H and Tsukruk V V. Liquid-crystalline processing of highly oriented carbon nanotube arrays for thin-film transistors. *Nano Lett*, 2006, 6: 1443-1448
- 48 Xie D, Lista M, Qiao G G, et al. Shear induced alignment of low aspect ratio gold

nanorods in newtonian fluids. J Phys Chem Lett, 2015: 3815-3820

49 Davis V A, Parra-Vasquez A N, Green M J, et al. True solutions of single-walled carbon nanotubes for assembly into macroscopic materials. Nat Nanotechnol, 2009, 4: 830-834

50 Zhang W, Lin J, Xu W, et al. SCStore: Managing scientific computing packages for hybrid system with containers. Tsinghua Sci Technol, 2017, 22: 675-681

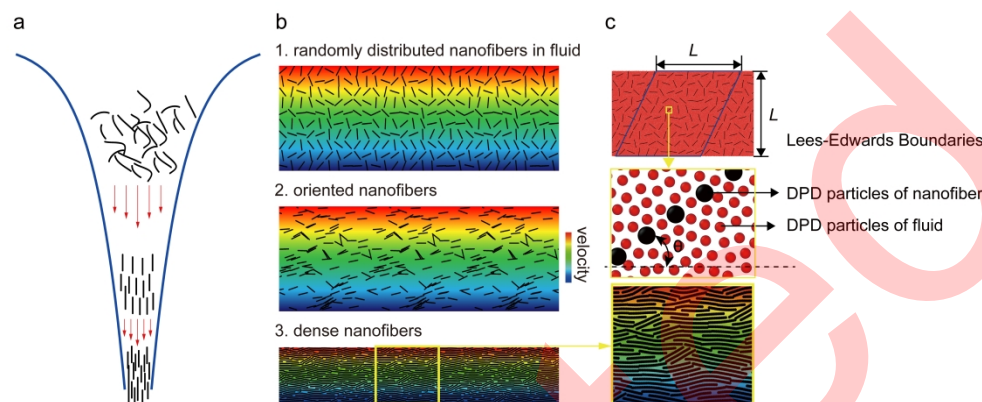


Figure 1

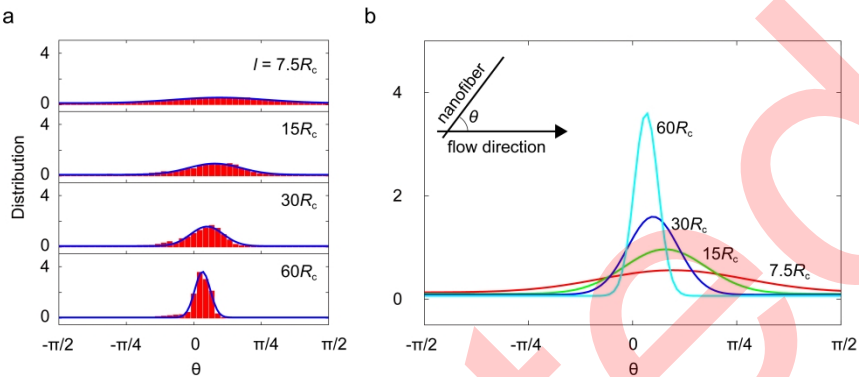


Figure 2

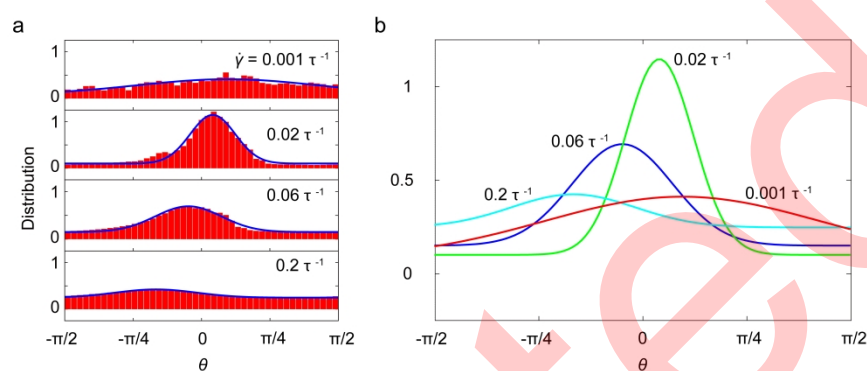


Figure 3

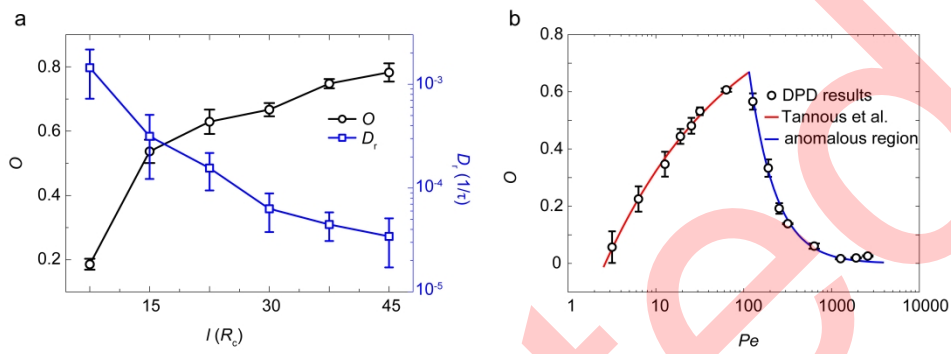


Figure 4

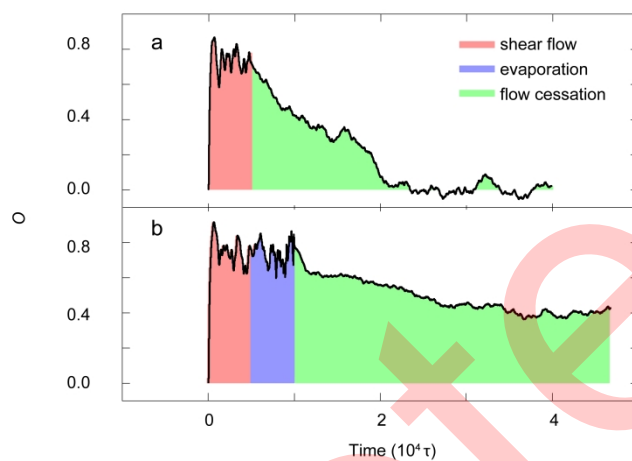


Figure 5

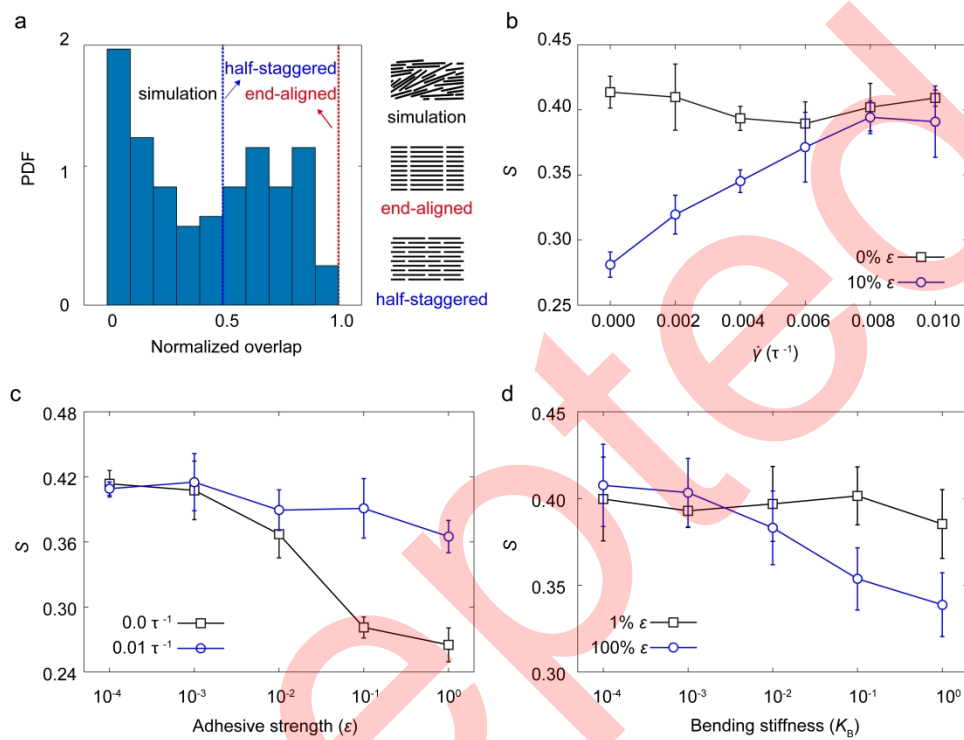


Figure 6

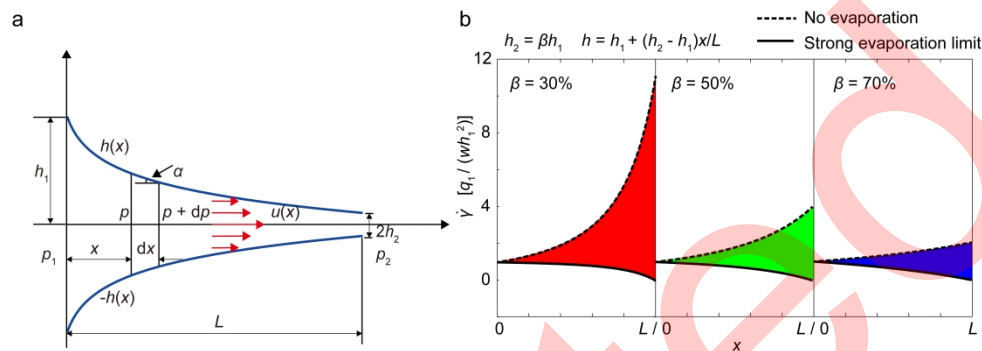


Figure 7

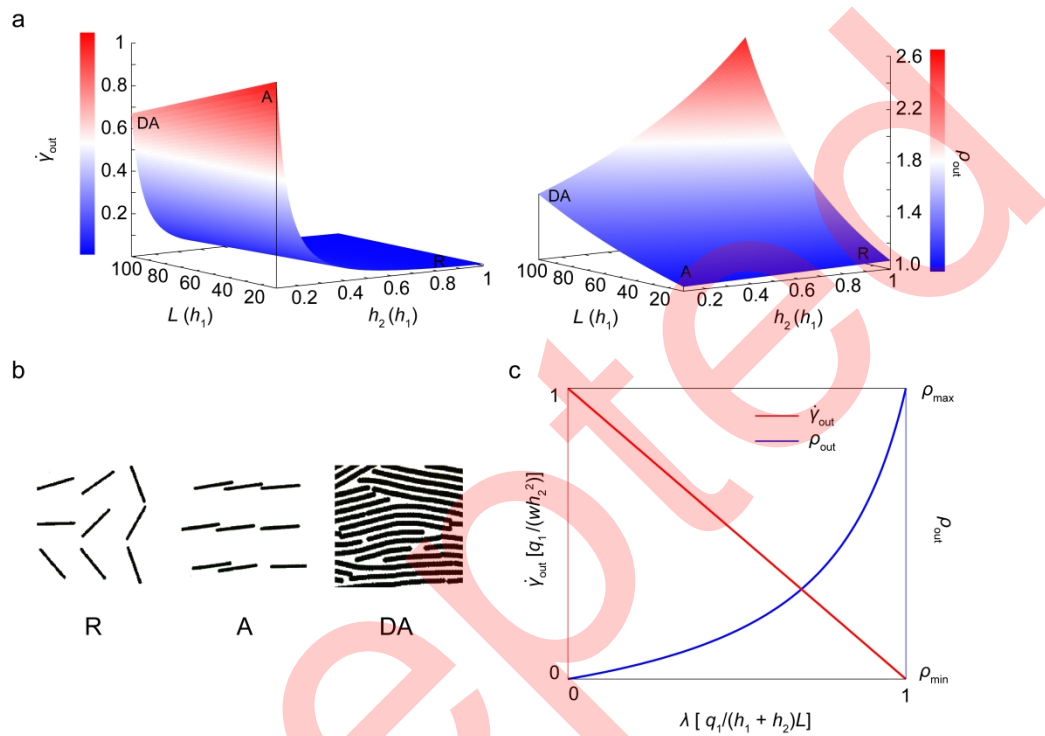


Figure 8